Composites

A new approach for preparation of metal-containing polyamide/carbon textile laminate composites with tunable electrical conductivity

Filipa Oliveira[1], Nadya Dencheva[1], Pedro Martins[2], Senentxu Lanceros-Méndez[2,3,4], and Zlatan Denchev[1,*]

[1] Institute for Polymers and Composites, University of Minho, 4800-058 Guimarães, Portugal

[2] Center/Department of Physics, University of Minho, 4710-057 Braga, Portugal

[3] BCMaterials, Basque Center for Materials, Applications and Nanostructures, UPV/EHU Science Park, 48940 Leioa, Spain

[4] IKERBASQUE, Basque Foundation for Science, Bilbao, Spain

ABSTRACT

Multiscale thermoplastic laminate composites based on polyamide 6 (PA6) dually reinforced by carbon fiber woven textile structures (CFT) and different micron-sized metal particles are prepared for the first time by microencapsulation strategy. In a first step, activated anionic ring-opening polymerization (AAROP) of ε-caprolactam is carried out in suspension, in the presence of different metal particles, to produce shell-core PA6 microcapsules (PAMC) loaded with 13–19% metal. In a second step, the loaded PAMC are distributed between CFT plies with fiber volume fractions $V_f = 0.25$ or $V_f = 0.50$ and then the ply arrays are consolidated by compression molding. Separately, metal-loaded PA6 hybrid composites are prepared by direct compression molding of PAMC and used to compare their properties to the CFT-metal laminates. Light- and scanning electron microscopy are used to study the morphology and the interfaces between the fillers and the polymeric matrix. These structural results are related to the mechanical behavior in tension and the electrical properties. A notable increase of the d.c. electrical conductivity in 7 orders of magnitude is observed for the CFT-metal laminates with respect to the neat PA6. This increase is accompanied by a 2.5–3.0 times growth of the Young's modulus and of the strength at break. It is concluded that the microencapsulation strategy can be applied to produce multifunctional CFT-metal-PA6 thermoplastic composites with tailored electrical and improved mechanical properties for advanced applications.

Address correspondence to E-mail: denchev@dep.uminho.pt

Introduction

Polymer composites reinforced by carbon fibers or textiles thereof (CFT) are being used for more than four decades in steadily increasing number of applications replacing metal-based structures in many industries. Traditional thermoset CFT composites based on epoxy, polyester or phenolic matrices deliver exceptional stiffness and strength, being at the same time very lightweight. Compared to most metals, CFT-reinforced thermosets offer superior mechanical properties/weight ratio, thus allowing manufacturers to reduce the weight per passenger in the modern aircrafts [1]. However, the CFT thermosets display limited extensibility and poor damage tolerance, especially at low operating temperatures [2]. Furthermore, common thermosetting resins polymerize to form the composite matrix only after reheating. Consequently, CFT thermosets have limited use in large-scale manufacturing requiring short production cycles, e.g., in automotive, electronics and electrical industries.

Much more attractive in the above cases can be the thermoplastic CFT composites (TPC/CFT). As compared to their thermoset counterparts, TPC/CFT display higher toughness of the matrix, higher impact resistance at low temperature, and significantly shorter manufacturing cycles. In addition to being lightweight, TPCs can be welded [3] and in some cases recycled by reprocessing [4], which is important in view of the rigorous requirements for environmental protection imposed in most industrialized countries.

Generally, fiber-reinforced TPCs are manufactured by melt-processing of the polymer matrix and the mineral reinforcement including well-established methods as prepreging [5], film stacking [6], preparation of powder-impregnated, comingled [7, 8], and braided hybrid yarns or cloths [2, 9]. The finished composite article is consolidated by different techniques including compression molding, pultrusion, autoclave processing, or tape placement. The common shortcoming of these approaches is the high viscosity of the melted polymer matrix material and the related insufficient wetting of the reinforcement resulting in weak matrix/reinforcement interface. To overcome these issues, special methods are applied with elevated costs of both raw materials and

manufacturing making them feasible only for high-performance applications.

An alternative way to produce TPCs is by reactive processing techniques, where the TPC is obtained in situ, through polymerization of low-viscosity monomers or oligomers in the presence of the reinforcements. This approach requires monomers able to produce high molecular weight polymers formed at sufficiently high conversions and without generation of byproducts. Among the polymerization types meeting these requirements, the most common is the ring-opening polymerization (ROP) [10] based on anionic or cationic mechanisms. Thus, polyamide-6 (PA6) can be produced through activated anionic ROP (AAROP) of the inexpensive ε-caprolactam (ECL). Strong bases such as metal caprolactamates are most often used as initiators of the process and imide group containing compounds as activators, whereby the polymerization process is completed in several minutes [11, 12]. Numerous studies exist on reactive processing toward polyamide thermoplastic composites through ionic polymerizations employing injection pultrusion [13, 14], reactive vacuum infusion [15, 16], reactive rotational molding [17, 18], resin transfer molding [19], and reaction injection molding [20]. A common disadvantage of the reactive processing methods, however, is the inevitable formation of low molecular weight fraction during the polymerization stage. It is impossible to remove and leads to the deterioration of the mechanical properties of the finished composite part.

An additional limitation of the CFT-reinforced thermosets and thermoplastics is the fact that the conventional matrix polymers are electric insulators that can be limiting for some applications. Hence, diverse methods have been used to improve this material property using chemical vapor deposition of copper thin films for metallization of the laminate [21], cold spray processes to deposit metal particles upon the laminate [22–24] or lay-up molding manufacturing methods [25] in which a metallic layer is cold-sprayed onto the CFT ply. Recently, Kong et al. have reported a hydrothermal method in which CuO nanostructures are grown on woven carbon fiber surface subsequently used to obtain a polymer laminate by vacuum-assisted resin transfer molding [26]. All these procedures require expensive and specific equipment with high processing costs, the part sizes and shapes being limited to the equipment geometry. Also, the adhesion at the metal-substrate interface

could be low if the substrate is not properly prepared for metallization.

This work suggests a novel two-stage process to produce TPC/CFT laminate composites based on PA6 that combines the advantages of the reactive processing and the carbon fiber metallization concept. First, metal-containing PA6 microcapsules (PAMC) are prepared via reactive microencapsulation process in which various types of finely divided metals are incorporated into PA6 particles formed during solution/precipitation AAROP of ECL monomer. Thus, pulverulent PA6 material free of low molecular weight fraction and optimal metal particles distribution can be produced. The latter is used in the second stage for powder-coating of CFT plies consolidated thereafter into polyamide TPC/CFT by compression molding. The morphology of the resulting multiscale composites was explored by light and scanning electron microscopy and correlated with their electrical conductivity, dielectric properties and mechanical properties in tension.

Experimental section

Materials

The ECL monomer with reduced moisture content for AAROP (AP-Nylon® caprolactam) was delivered from Brüggemann Chemical, Germany. As polymerization activator Brüggolen C20® from Brüggemann Chemical, Germany (C20) was used. According to the manufacturer, it contains 80 wt% of blocked di-isocyanate in ECL. The initiator sodium dicaprolactamato-bis-(2-methoxyethoxo)-aluminate (Dilactamate®, DL) was purchased from Katchem, Czech Republic, and used without further treatment. Powdered Cu (> 99.5%, grain size < 40 μm), Al (> 93%, grain size < 100 μm), and Mg (> 99%, grain size < 100 μm) were supplied by Sigma-Aldrich. The soft, non-insulated carbonyl Fe powder (> 99.5, average grain size 3–5 μm) was kindly donated by the BASF Group, Germany. The plain-weave CF textile structure with area density of 195 g/m^2 was supplied by PIEP—Pólo de Inovaçao em Engenharia de Polímeros, Portugal. All CFT textile structures were cut to the shape of the mold. Toluene, methanol, and other solvents, all of "puriss" grade, were purchased from Sigma-Aldrich and used as received.

Sample preparation

The loaded PAMC were produced by solution-precipitation AAROP of ECL performed as described in detail previously [27–30]. Typically, about 0.5 mol of ECL and the desired amount of Al, Cu, Fe, or Mg powder (10 wt% in respect to ECL) were added to 100 mL of 1:1 toluene/xylene mixture while stirring, under nitrogen atmosphere, refluxing the reaction mixture for 10–15 min. Subsequently, 3 mol% of DL and 1.5 mol% of C20 were added at once. The reaction time was always 2 h from the point of catalytic system addition, maintaining the temperature in the 125–135 °C range at a constant stirring of ca. 800 rpm. The metal-loaded PAMC was formed as a fine powder with metallic luster typical of the respective metal load (Fig. 1a). They were separated from the reaction mixture by hot vacuum filtration, washed several times with methanol, and dried for 30 min at 80 °C in a vacuum oven. The yields of empty PAMC were 56% (in respect to ECL) and 45–49% for the loaded PAMC (Table 1).

Two sample sets were produced from the loaded PAMC. By their direct compression molding, PA6-metal hybrid composite plates were prepared and designated as P-series (Table 2). In the same way, empty PAMC were compression molded to anionic PA6 plates (P-PA6) and used as reference sample. The PA6 laminate composites dually reinforced by metal and CFT (the L-series in Table 2) were prepared by compression molding of empty PAMC with CFT (L-PA6 25 and L-PA6 50) and metal-loaded PAMC with CFT (the rest of the samples in the L-series, Table 2), the numbers indicating $V_f = 0.25$ and $V_f = 0.50$. Compression molding was performed in a hydraulic hot press (Moore, UK) using a mold with dimensions 70 × 70 × 2 mm, pressing for 10 min at 230 °C at a pressure of ca. 5 MPa. To determine the number of CFT plies necessary to obtain the corresponding V_f values, the following equation was applied:

$$V_f = \frac{A_w \cdot n}{\rho_f \cdot t} \tag{1}$$

where V_f is the volume fraction of the reinforcements, A_w the area density (g/m^2) of the textile structure used, n is the number of plies, ρ_f is the density of the carbon fibers (g/m^3) and t is the laminate thickness [31]. Figure 1 shows the visual aspect of PAMC (Fig. 1a) of different molded composite plates from
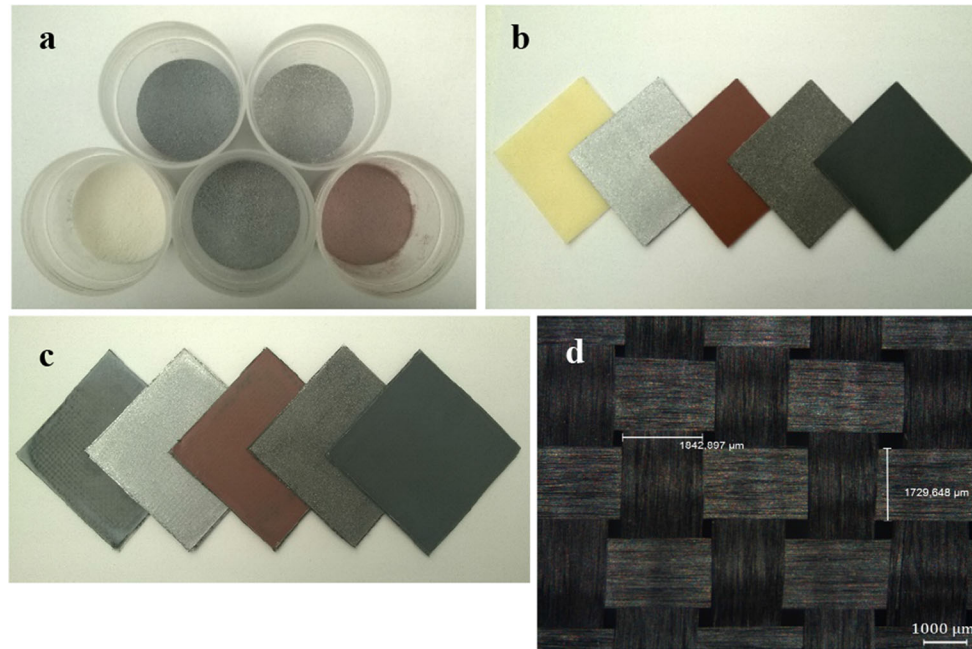
Figure 1 Visual aspect of the materials used: **a** PAMC with metal payloads; **b** hybrid metal composites (P-series), 68 × 68 × 2 mm, from left to right: PA6, P-Al 10, P-Cu 10, P-Mg 10, P-Fe 10; **c** metal/CFT-reinforced laminate composites (L-series), 68 × 68 × 2 mm: L-PA6 25, L-Al 25, L-Cu 25, L-Mg 25, L-Fe 25; **d** stereoscopic image of a plain-weave CFT ply. (For better visualization of the colors in this figure, the reader is referred to the web version of this article).

Table 1 PAMC: sample designations, composition and polymerization yield

Sample designation	Load (wt%)[a]	PAMC yield (wt%)[b]	Real load, RL (wt%)[c]
PA6	–	56.0	–
Al10	10	45.1	19.4
Cu10	10	48.6	17.6
Mg10	10	48.9	13.0
Fe10	10	49.2	13.4

[a]In respect to ECL during AAROP

[b]In respect to the sum of the weight of ECL and fillers

[c]Determined by TGA according to Eq. 2

the P- and L-series (Fig. 1b, c), and of the plain-weave CFT ply (Fig. 1d).

Characterization techniques

Reflected light microscopy (RLM) observation of laminate composites (L-series) was performed in an Olympus BH-2 microscope (Olympus Corp. Japan) equipped with a Leica DFC200 (Leica Microsystems, Germany) digital camera. Selected laminate samples were embedded in epoxy resin suitable for light microscopy. After curing, the surface of the embedded composite was polished in a Minitech 233 manual polishing machine (Presi, France) using a series of abrasive papers to obtain a transparent and glossy surface without scratches.

The scanning electron microscopy (SEM) studies were performed in a NanoSEM-200 apparatus of FEI Nova (USA) using mixed secondary electron/back-scattered electron in-lens detection. The composite samples were observed after sputter-coating with Au/Pd alloy in a 208 HR equipment of Cressington Scientific Instruments (UK) with high-resolution thickness control. The PA6-reinforced laminates (L-series) were observed after cryofracture in liquid nitrogen.

The effective inorganic load in PAMC RL was established by means of thermogravimetric analysis

Table 2 Designation of all composite materials prepared by compression molding with and without CFT. P-series hybrid plates; L-series: PA6/CFT laminate

Sample designation	Real metal load (%)[a]	CFT load (%)	No. CFT plies
P-PA6	–	0	0
L-PA6 25		25	4
L-PA6 50		50	9
P-Al10	19.4	0	0
L-Al25		25	4
L-Al50		50	9
P-Cu10	17.6	0	0
L-Cu25		25	4
L-Cu50		50	9
P-Mg10	13.0	0	0
L-Mg25		25	4
L-Mg 50		50	9
P-Fe10	13.4	0	0
L-Fe25		25	4
L-Fe50		50	9

[a]Determined by TGA according to Eq. 2

(TGA) in a Q500 gravimetric balance (TA Instruments, USA) heating the samples to 600 °C at 10 °C/min in a nitrogen atmosphere. The RL value in PAMC was calculated according to Eq. (2):

$$RL = R_i - R_{PA6} [\%] \qquad (2)$$

where R_{PA6} is the carbonized residue at 600 °C of empty PAMC and R_i—represents the carbonized residue of the respective loaded PAMC measured by TGA.

Tensile tests were performed in a Shimadzu Autograph AGS-X Series (Japan) at 23 ± 2 °C with a standard load cell of 50 kN and a constant crosshead speed of 50 mm/min. From the different composite plates of the P- and L-series, standard specimens were cut out according to DIN 53504-S3A. At least five specimens of each sample were studied to calculate the average values of the tensile characteristics and the respective standard deviations. The engineering stress σ was determined as the ratio of the tensile force to the initial cross-section of the sample. The engineering strain ε was determined as the ratio of the sample gauge length at any time during drawing to that before drawing. The values of the Young's modulus E were obtained from the initial slope of the strain–stress curves (up to 1% strain). In all cases, conditioned samples stored for ca. 30 days at 23 °C and 65% relative humidity were tested.

The improvement factor IF for E and σ_{br} values were calculated according to Eq. (3):

$$IF = \frac{P_i - P_{PA6}}{P_{PA6}} \cdot 100 [\%] \qquad (3)$$

where P_i is the respective parameter of the composite material and P_{PA6} is the same parameter of the neat PA6 matrix.

Electrical current/voltage measurements were performed in a Keithley 487 pico-amperemeter/voltage source (Keithley Instruments Inc., USA) between − 10 and + 10 V using voltage increasing and/or decreasing modes. To rule out interferences due to external electric field, all measurements were performed in a Faraday cage. From the slope of the graphs (straight lines for Ohmic materials), the resistance $R[\Omega]$ was determined, from which the resistivity ρ [Ω m] and conductivity σ [S/m] were calculated according to Eq. (4):

$$\sigma = \frac{1}{\rho} = \frac{1}{R} \cdot \frac{d}{A} \qquad (4)$$

where A is the area of the gold electrodes (5 mm in diameter) deposited by sputtering on both free surfaces of each sample, and d the thickness of the composite. Four measurements in different parts of each molded sample were performed taking the arithmetical mean as a final value of conductivity.

The dielectric permittivity ε' was obtained from the geometry of the samples in the shape of a parallel plate capacitor (circular electrodes of 5 mm diameter and sample average thickness of 600 μm) and the measurement of the capacity and the loss factor $tan\ \delta$ with a QuadTech (Marlborough, USA) model 1920

precision LCR meter at room temperature and pressure, at frequencies between 100 Hz and 1 MHz. The permittivity ε' of the samples was determined according to Eq. (5):

$$C = \varepsilon' \cdot \varepsilon_0 \cdot \frac{A}{d} \tag{5}$$

where A is the area of the capacitor plates with capacitance C, d is the sample thickness, and ε_0 is the dielectric permittivity of vacuum. The electrical d.c. conductivity σ, the values of permittivity ε', dielectric loss ε'', and loss factor tan $\delta = \varepsilon'''/\varepsilon''$ were obtained for all molded composites.

Results and discussion

Synthesis of the loaded PAMC

The synthesis of metal-loaded PAMC via AAROP was described in detail in [28]. According to this and previous studies [32–34], it can be hypothesized that during the anionic polymerization of ECL the microsized metal particles are entrapped into viscous oligomer droplets formed by the growing PA6 polymer molecules. After reaching some critical molecular mass and various acts of coalescence, these droplets crystallize transforming into porous PA6 shell that embeds one or more metal particles. The latter can possibly nucleate the PA6 crystallization, thus forming the loaded PAMC. The transformation of the viscous droplets into loaded microcapsules without formation of lumps requires an optimized stirring rate of ca. 800 rpm, maintaining the molar ratio DL/C20 = 2 and keeping the temperature of AAROP below 135 °C.

Table 2 shows the designations of the prepared loaded PAMC samples, the corresponding polymerization yields, and the concentrations of metal filler with respect to ECL introduced during AAROP. For all samples, the real filler concentration RL was determined by TGA according to Eq. (3). Since the polymerization yields were in the range of 50% in respect to ECL, the real metal loads in PAMC were expected to be almost twice as high as in the starting reaction mixture. This was the case with the Al- and Cu-containing PAMC where RL values of 18–19% were observed. The much smaller RL in the Mg-loaded PAMC can be attributed to the very low density of the Mg particles, resulting in their loss during

AAROP that is performed under reflux and nitrogen flow. In the case of the PAMC containing Fe, a part of the metal particles gets stuck to the magnetic stirrer and is therefore not involved into microcapsules that resulted in lower RL.

Microscopy studies

The scanning electron micrographs in Fig. 2 present information about the size and shape of the used metal particles. The Al and Mg particles (Fig. 2a, c) are shaped as platelets with maximum sizes of 100–350 and 300–400 µm, respectively, and thicknesses of ca. 1–10 µm. The Cu particles (Fig. 2b) display complex dendritic shapes with sizes in the 20–40 µm range, and the Fe particles (Fig. 2d) are spherical with sizes between 1 and 5 µm.

The morphological characterization of neat PAMC and of such loaded with up to 5–6 wt% Al, Cu, and Fe particles were reported in [29]. Figure 2f–i represent similar PAMC but loaded with more than 3 times more metal of each type. With the exception of the PAMC containing Al (Fig. 2f) and Mg (Fig. 2h), all other loaded PAMC and the empty PA6 microcapsules (Fig. 2e) represent aggregates of several, partially fused spheres with typical diameters of 5–10 µm that form final particles of 20–30 µm for empty PAMC to 30–50 µm for the Cu10 samples (Fig. 2g). In the case of the Al10 and Mg 10 sample (Fig. 2f, h), the in situ forming PA6 coats the metal platelets. Therefore, it can be supposed that the size and shape of the loaded PAMC is determined by the morphology of the initial metal particles. The large Al and Mg platelets are covered by polyamide sheath during the AAROP. In the case of the smaller Fe and Cu particles, one or more of them are included into the viscous particles produced in AAROP that after coalescence form the final PAMC. In the case of Fe-loaded PAMC (Fig. 2i), the formation of cylindrical structures should be ascribed to auto-assembly of magnetized Fe particles and their subsequent coating by anionic PA6 in the process of microencapsulation during which the reaction media is stirred magnetically. [29].

The stereoscopic image of the plain-weave CFT used in the production of molded laminate composites shows the isotropic arrangement of the carbon filament bundles in two perpendicular directions (Figure 1d). The RLM images of selected dually reinforced laminate composites prepared by
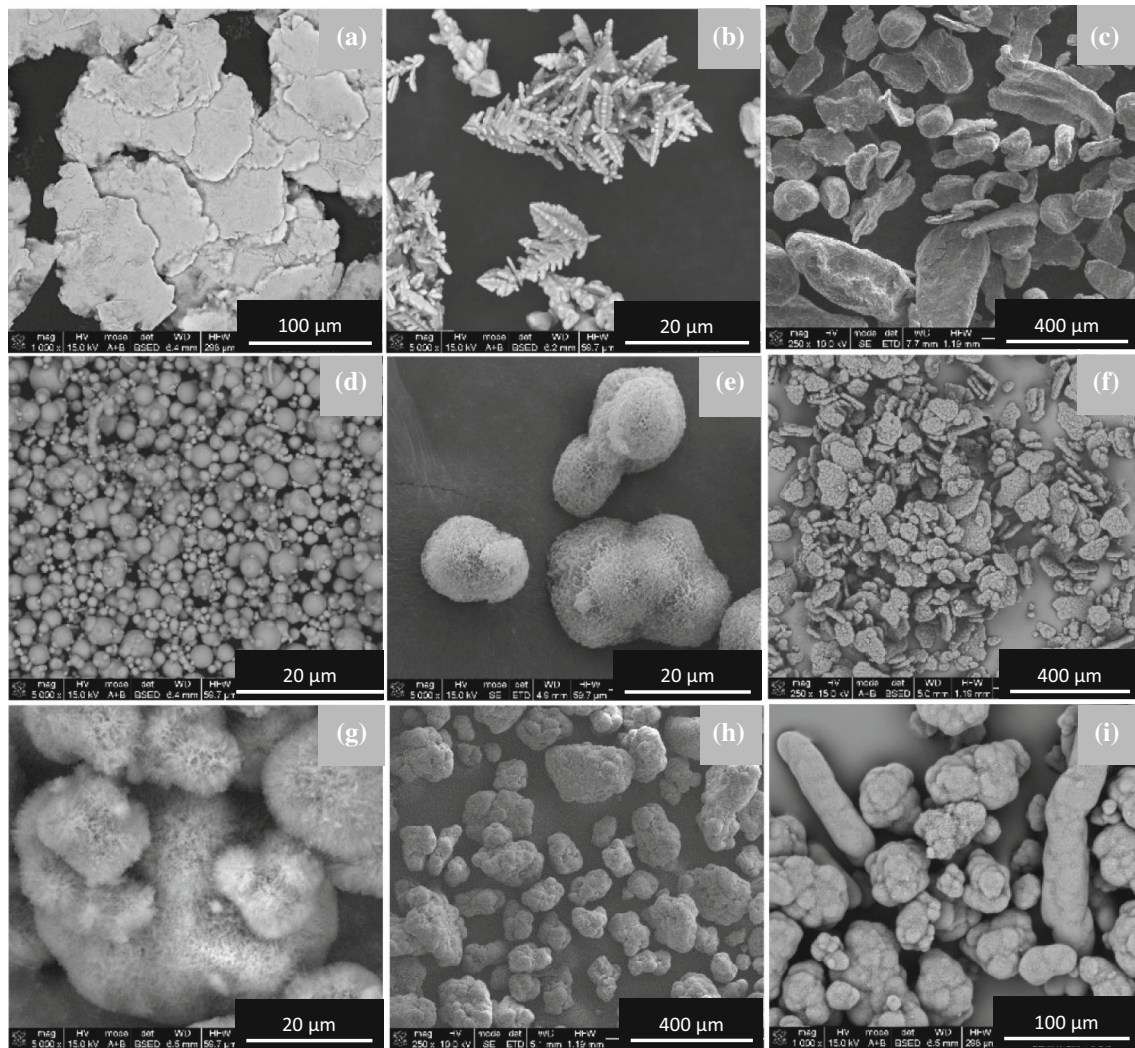
Figure 2 Selected SEM micrographs of neat metal particles and metal-loaded PAMC: **a** Al; **b** Cu; **c** Mg; **d** Fe; **e** empty PAMC; **f** Al10; **g** Cu10; **h** Mg10; **i** Fe10.

consolidation of metal-loaded PAMC and CFT in a volume fraction V_f = 0.25 are presented in Fig. 3. It can be observed that in all of these systems containing four CFT plies, good distribution of the metal particles within the five PA6 matrix zones was achieved. The relatively low density of the Al and Mg and the bigger sizes of these particles leads to very dense packing of the PA6 matrix interlayers with metal (Fig. 3b, c, h, i, respectively). The heavier Cu and Fe particles are included in lower concentrations in the interlayers making them hardly visible in the latter case due to the smaller sizes of the Fe particles (3–5 μm) (Fig. 3f, g), against the 20–25 μm size of Cu particles (Fig. 3d, e). A general feature of all images in Fig. 3 is that no damage of the CFT plies is caused during consolidation and that the well-distributed

metal particles are also in good contact with the carbon filaments from CFT, especially in the Al- and Mg-containing laminates. The arrows in Fig. 3a, b, h indicate the thickness of the laminate samples, which is close to 2 mm.

To visualize better the metal-loaded PA6 matrix/CFT interface in the same laminate composites and the morphology of the carbon fibers, SEM studies were performed using cryofractured samples (Fig. 4). In general, the micrographs provide proofs for good and relatively homogeneous impregnation of the CFT by the PA6 matrix material without metal load (Fig. 4a) or containing high metal loads (Fig. 4b–f). The latter five images display also carbon filaments from CFT with average diameters of 7.0–7.5 μm. In all metal-containing laminates, it was possible to
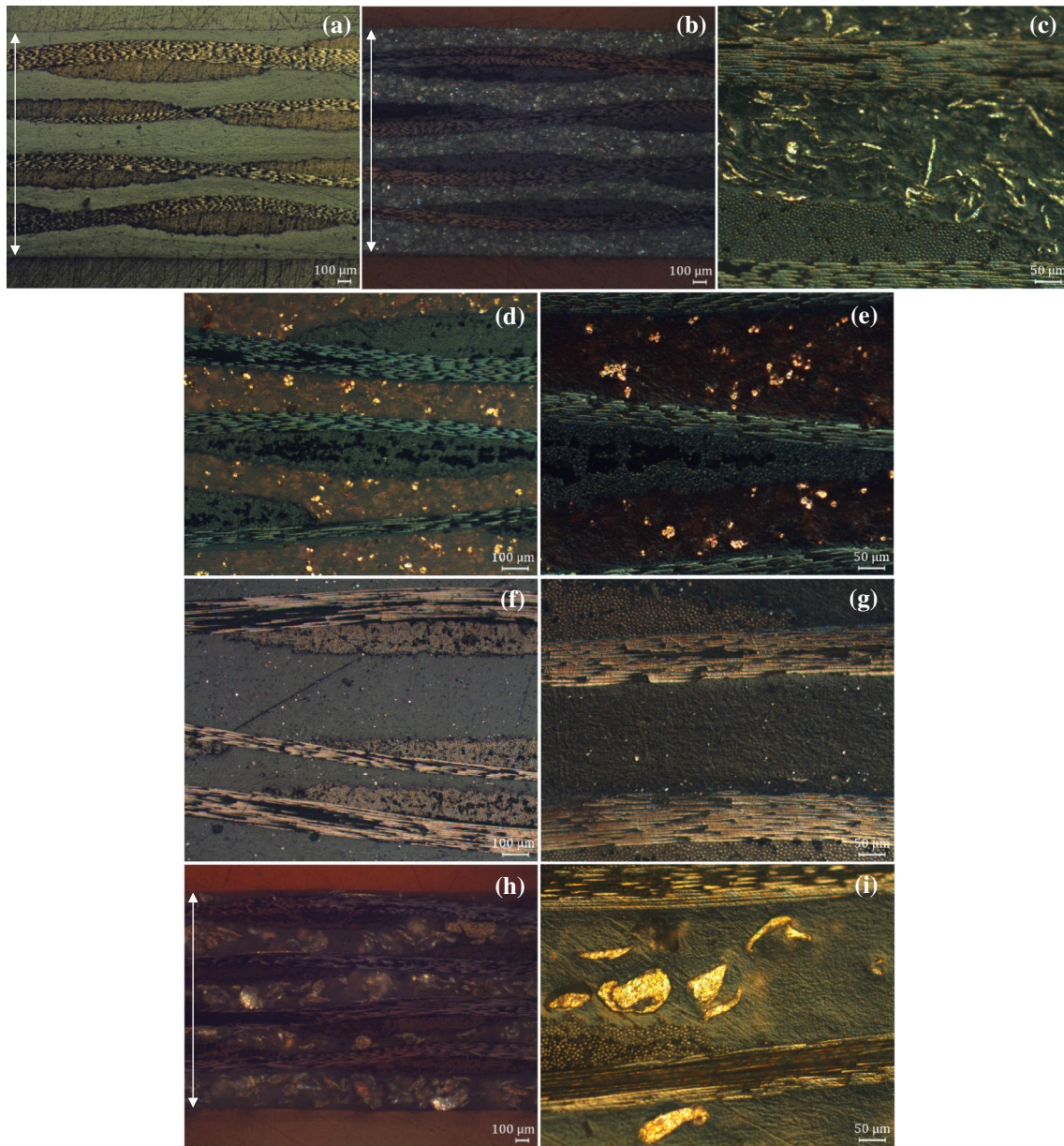
Figure 3 Selected RLM images of molded laminate composites with V_f = 0.25 prepared from metal-loaded PAMC: **a** L-PA6 25; **b** L-Al25; **c** close view of the distribution of Al particles in sample (**b**); **d** L-Cu 25; **e** magnification of the sample (**d**); **f** L-Fe25; **g** magnification of sample (**f**); **h** L-Mg25; **i** close view of sample (**h**). For sample designation, see Table 2. White arrows in images **a**, **b**, **h** delimit the thickness of the laminate cross-section. (For visualization of the colors in this figure, the reader is referred to the web version of this article).

identify by EDX the specific emission peaks of the respective metal particles, well incrusted by matrix material in the interlayers between the CFT plies (Fig. 4).

Thermal properties

All metal-loaded PAMC and corresponding composites were analyzed by TGA. One of the purposes was the determination of the real metal content RL in either PAMC or the molded plates thereof taking in account the carbonized residue at 600 °C. As expected, the RL in PAMC and the respective molded
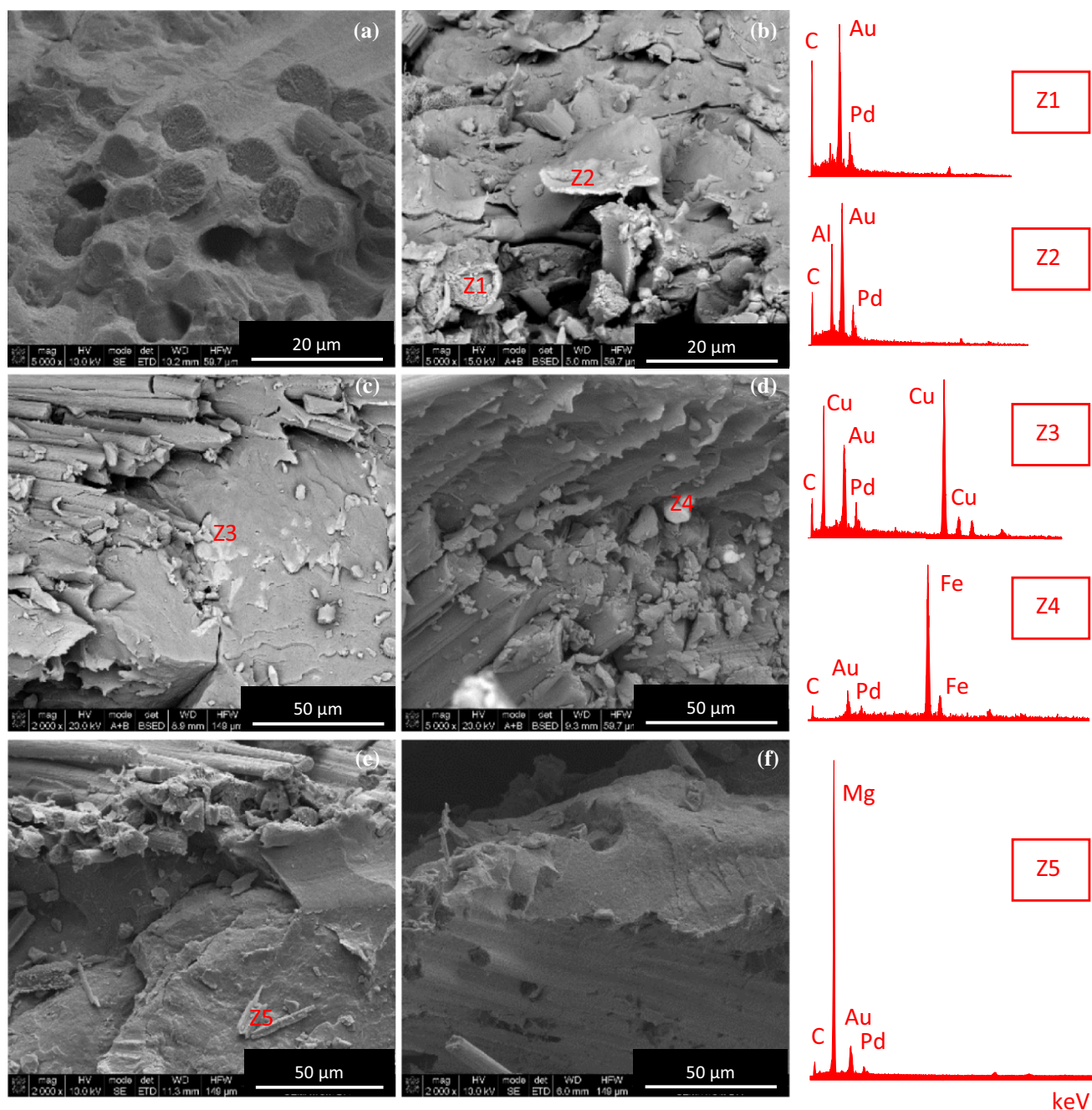
Figure 4 Selected SEM images of molded laminate composites prepared from metal-loaded PAMC: **a** L-PA6 50; **b** L-Al50; **c** L-Cu50; **d** L-Fe25; **e** L-Mg25; **f** L-Mg50. For sample designation, see Table 2. The graphs in the right column show the EDX emission curves in the Z_i sites.

plates are basically the same (Table 3). Small loss of metal during the compression molding was observed only in the Mg-containing plates.

Figure 5 displays the weight retention TGA curves, and Table 3 summarizes the numerical data of the thermal degradation derived from the TGA curves. The metal-loaded PAMC (Fig. 5a) and the respective

molded plates (Fig. 5b) display similar thermal stability as compared to the neat PA6 counterparts. Judging from the temperature of 10% weight loss $T_{10\%}$ and that of the maximum degradation rate T_{MDR} in Table 3, some stability improvement is observed in the systems comprising the large and less dense Al and Mg particles. At the same time, in the Cu- and

Table 3 Thermal degradation by TGA of PAMC and the respective compression molded composites (plate)

Sample designation		Temperature of 10% weight loss (°C)	T_{MDR} (°C)	Residue at 600 °C R_i (%)	Real load RL (%)
PA6	PAMC	295.4	339.3	1.4	–
	Plate	303.8	354.0	1.1	–
Al10	PAMC	317.0	358.5	20.8	19.4
	Plate	323.8	357.5	20.6	19.5
Cu10	PAMC	290.0	335.9	19.0	17.6
	Plate	300.9	321.5	18.8	17.7
Mg10	PAMC	331.3	347.1	14.3	13.0
	Plate	309.7	345.6	13.7	12.7
Fe10	PAMC	286.7	334.3	14.8	13.4
	Plate	297.8	319.4	14.7	13.6

T_{MDR} = temperature of maximal degradation rate obtained from the 1st derivative of the TGA curves in Fig. 5
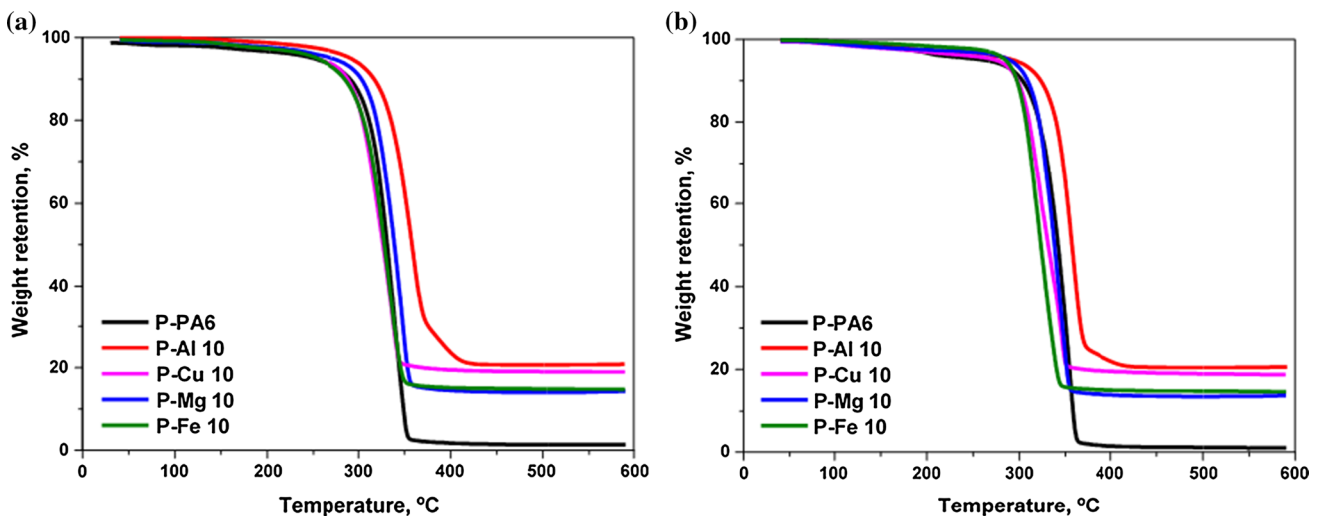

Figure 5 Integral TGA curves of: **a** metal-loaded PAMC and **b** molded plates thereof (P-series) obtained in inert N_2 atmosphere.

Fe-containing systems the thermal degradation is more pronounced, especially in the molded plates. This effect can be explained with the thicker packing of the PA6 matrix with touching to one another Al and Mg particles that was visualized in the microscopic studies in Fig. 3. This leads to an easier dissipation of the heat during the TGA experiment and, consequently, in higher degradation temperatures. On the contrary, loading the PA6 matrix with lower volume fractions of the smaller Cu and Fe particles that remain isolated seems to have an opposite effect attributable to overheating localized around each metal particle.

Tensile properties of the composites

Representative stress–strain curves of the hybrid plates obtained from metal-loaded PAMC (P-series in Table 4) and of the dually reinforced laminates with CFT volume fraction $V_f = 0.25$ (L-series in Table 4) are presented in Fig. 6a, b, respectively. Table 4 shows the data of the Young's modulus E, stress at break σ_{br} and deformation at break ε_{br}, extracted from the stress–strain curves of all samples, as well as the improvement factors (I)F for the E and σ_{br} values.

The stress–strain curves of plates produced from empty PAMC and from Cu- and Fe-loaded PAMC (Fig. 6a, samples PA6, P-Cu10, P-Fe10) display clear Hookean elasticity regions followed by a ductile behavior with well-expressed yield point at

Table 4 Results from the tensile strength experiments

Sample designation	Young's Modulus, E (GPa)	IF[a] (%)	Tensile strength at break, σ_{br} (MPa)	IF[a] (%)	Deformation at break, ε_{br} (%)
PA6	1.25 ± 0.07	–	63.7 ± 4.95	–	20.5 ± 4.60
P-Al10	1.96 ± 0.08	57	58.3 ± 3.91	− 8	4.73 ± 0.38
P-Cu10	1.47 ± 0.01	18	55.1 ± 2.19	− 13	19.7 ± 1.96
P-Mg10	1.78 ± 0.03	42	66.1 ± 1.53	4	6.27 ± 0.34
P-Fe10	1.47 ± 0.03	17	65.4 ± 1.58	3	13.8 ± 1.18
L-PA6 25	4.22 ± 0.24	238	251.2 ± 22.4	294	14.0 ± 2.01
L-Al25	4.88 ± 0.10	290	271.9 ± 12.1	327	13.8 ± 0.86
L-Cu25	4.45 ± 0.24	256	249.1 ± 21.2	291	11.3 ± 1.37
L-Mg25	4.76 ± 0.57	280	260.0 ± 14.2	208	13.0 ± 0.21
L-Fe25	5.14 ± 0.37	311	239.0 ± 6.1	276	10.8 ± 0.48

[a]In respect to neat anionic PA6 plate obtained from empty PAMC, calculated according to Eq. 3
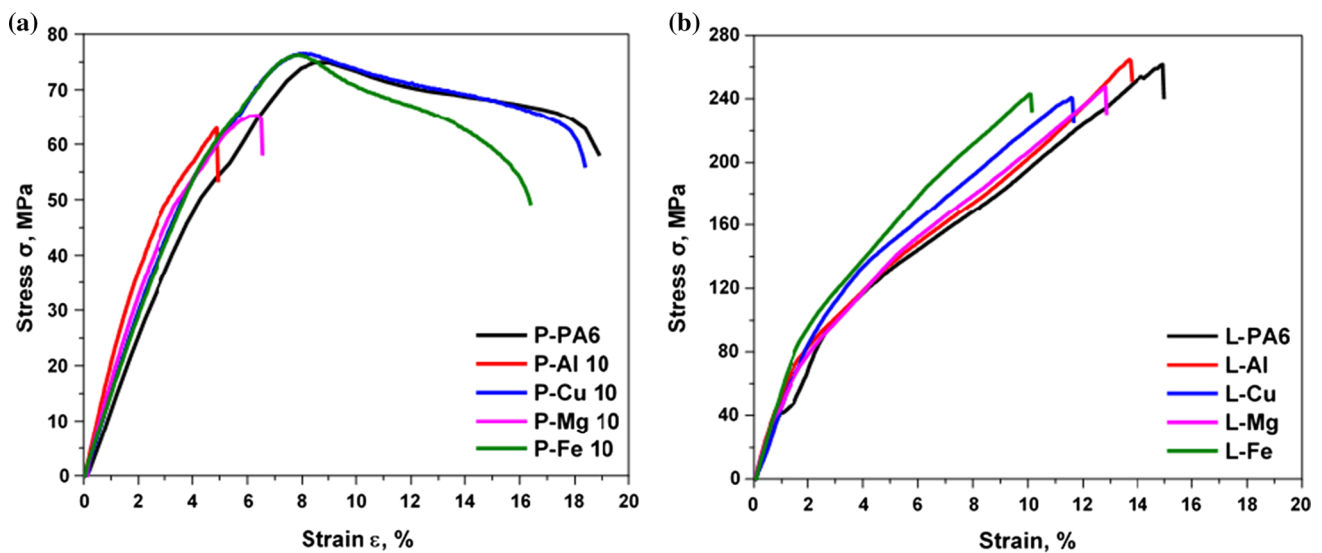

Figure 6 Stress–strain curves from the tensile tests of: **a** hybrid plates obtained from metal-loaded PAMC; **b** dually reinforced laminates prepared with metal-loaded PAMC and $V_f = 0.25$ of CFT.

Table 5 Electrical properties of hybrid composites prepared from metal-loaded PAMC

Matrix composition	Conductivity, σ_{DC} (S/m) $\times 10^{10}$	Dielectric constant[a], ε'	Loss factor[a], $\tan \delta \times 10^2$
PA6	5.22 ± 0.14	6.64 ± 0.20	5.3 ± 0.08
P-Al10	35.0 ± 1.70	22.9 ± 2.55	109 ± 13
P-Cu10	15.6 ± 1.76	24.0 ± 1.41	108 ± 10
P-Mg10	47.8 ± 3.78	23.6 ± 1.48	129 ± 8
P-Fe10	25.2 ± 3.82	24.5 ± 0.35	127 ± 8

[a]Values obtained at 1 MHz

σ = 70–75 MPa and ε = 8–9% strain, the deformation at break reaching 17–19%. The Young's moduli calculated for the two metal-containing samples of 1.47 GPa are only slightly higher than that of the neat PA6 (Table 4). These three samples display curves with a plateau called also "cold flow," which is typical for

Table 6 Electrical properties of dually reinforced laminate composites

Matrix composition	Conductivity, σ_{DC} (S/m)		Dielectric constant[a], ε'		Loss factor[a], tan δ	
	V_f = 25%	V_f = 50%	V_f = 25%	V_f = 50%	V_f = 25%	V_f = 50%
PA6	5.22E − 10 ± 1.40E − 11		6.64E + 00 ± 1.98E − 01		5.26E − 02 ± 7.78E − 04	
L-PA6	5.21E − 08 ± 3.60E − 09	3.60E − 07 ± 2.55E − 08	1.74E + 01 ± 4.24E − 01	2.14E + 01 ± 7.07E − 02	1.37E − 02 ± 1.34E − 03	1.32E − 02 ± 1.06E − 03
L-Al	3.02E − 07 ± 2.81E − 08	2.67E − 03 ± 4.88E − 04	1.77E + 01 ± 9.19E − 01	2.04E + 01 ± 4.24E − 01	1.19E − 02 ± 1.41E − 04	1.50E − 02 ± 3.11E − 03
L-Cu	2.08E − 07 ± 1.51E − 08	2.93E − 03 ± 3.96E − 04	1.76E + 01 ± 2.12E − 01	2.05E + 01 ± 3.54E − 01	1.56E − 02 ± 9.19E − 04	1.00E − 02 ± 2.52E − 03
L-Mg	3.21E − 03 ± 1.29E − 04	4.37E − 03 ± 1.04E − 04	1.80E + 01 ± 9.19E − 01	2.10E + 01 ± 4.95E − 01	9.77E − 03 ± 1.46E − 03	1.46E − 02 ± 2.83E − 04
L-Fe	4.32E − 03 ± 3.52E − 04	4.61E − 03 ± 2.07E − 04	1.67E + 01 ± 2.83E − 01	2.08E + 01 ± 7.07E − 02	1.49E − 02 ± 7.07E − 04	1.53E − 02 ± 7.78E − 04

[a]Values obtained at 1 MHz

Figure 7 Dielectric permittivity, ε' and loss factor, tan δ as a function of frequency in: **a**, **b** hybrid plates obtained from metal-loaded PAMC; **c**, **d** dually reinforced laminates prepared with metal-loaded PAMC and CFT with V_f = 0,25; **e**, **f** dually reinforced laminates prepared with metal-loaded PAMC and CFT with V_f = 0,50. For sample designation, see Table 2.

viscoelastic performance. At the same time, no cold flow is observed in the hybrid plates denoted as P-Al10 and P-Mg10. They show Hookean elasticity and a brittle fracture with ε_{br} values of 6–7% and σ_{br} below 65 MPa, i.e., lower than those of the neat PA6. The E-values of these two hybrids, however, are with 57 and 42% higher than those of the matrix PA6. These results can be related with the sizes of the metal particles used: It is observed that high E-values are caused by the larger and most densely packed Al and Mg particles, whereas the smaller Cu and especially Fe particles do not change the stress–strain profile and increase only slightly the Young's modulus.

As expected, the introduction of CFT plies significantly increases the E and σ_{br} values (in average by 208–325%, Table 4) accompanied by the appearance of strain-hardening regions in all stress–strain curves (Fig. 6b). No yield point or viscoelastic regions are observed. This behavior was expected as being typical for the textile-reinforced PA6-based TPC produced by AAROP [20, 30]. All metal-containing laminates show E-values being significantly better than the L-PA6 25 control sample, i.e., a synergetic effect between the CFT and metal powder reinforcements is observed. As regards the ultimate strength σ_{br}, the metal/CFT synergism is clearly evidenced only with the Al- and Mg-containing laminates.

Further improvement in the mechanical properties of these dually reinforced TPC/CFT composites can be expected after optimization of the volume fractions and types of the CFT reinforcements, as well as the parameters of the consolidation process—pressure, temperature and time duration.

Electrical conductivity and dielectric properties

The d.c. electrical conductivity σ, real component of the dielectric permittivity ε', and the loss factor $tan\ \delta$ were determined for all composites produced from
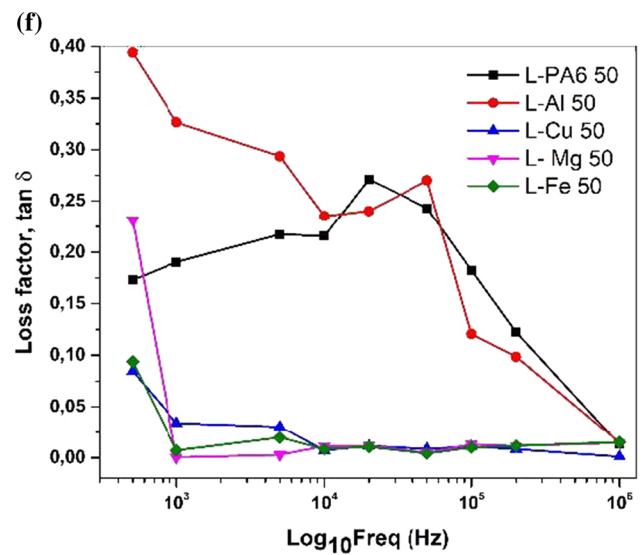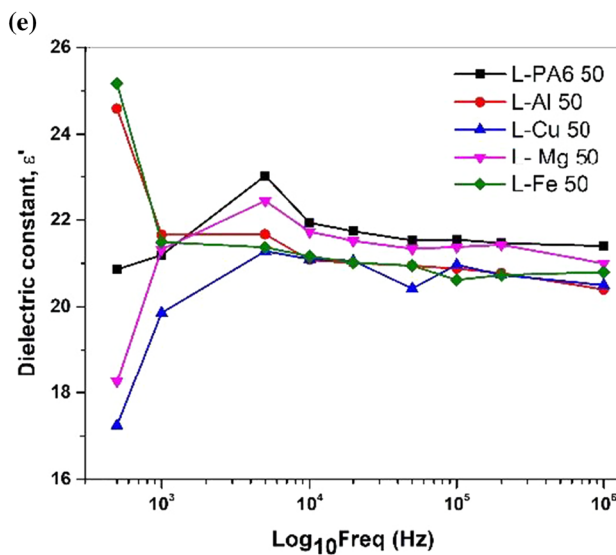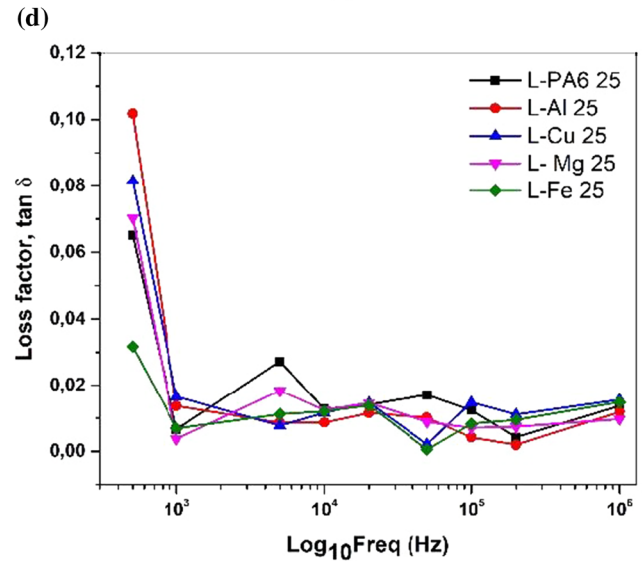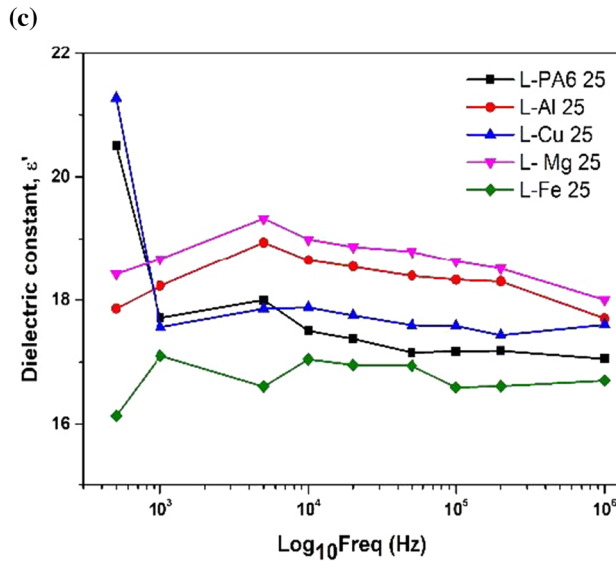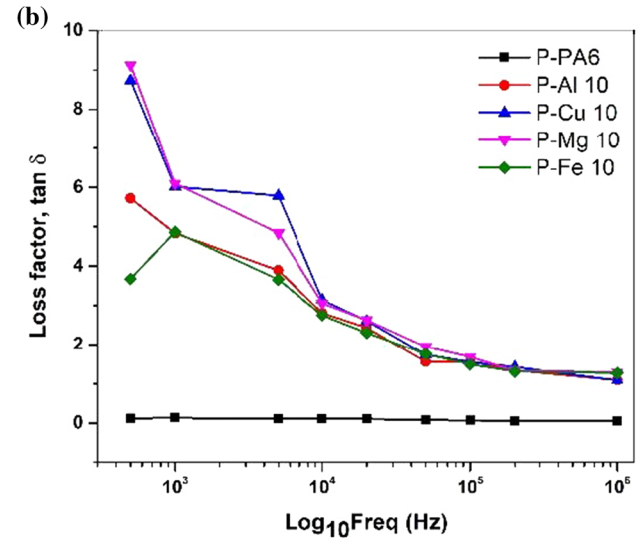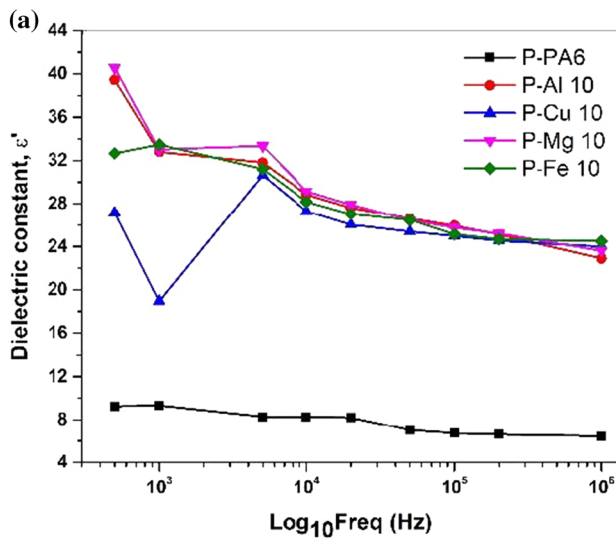
compression molded PAMC using Eqs. 4 and 5 and are summarized in Tables 5 and 6.

The data in Table 5 confirm previous findings [28] reporting that metal-containing PA6 hybrids produced by molding of PAMC with real loads of metal microparticles in the range of 1–30 wt% are still insulators with σ values in the range of 10^{-9} S/m, i.e., almost identical to that of the PA6 matrix. This effect was explained with a Maxwell–Wagner–Sillars-type polarization typical for multiphase dielectrics, in which the resistivity of the phases is quite different [35, 36]. The presence of plain-weave CFT along with the Al, Cu, Fe and Mg content with effective loads up to 19% (in respect to the PA6 matrix) apparently eliminates the polarization at the metal/PA6 interface. This causes a notable growth of the electrical conductivity σ in 7 orders of magnitude (Table 6). It should be noted that in the L-PA6 25 control laminate sample not containing metal particles this increase was reduced to 2 decades only. In view of this fact, the largely increased conductivity of the dually reinforced metal-CFT polyamide laminates should be assigned to the very good distribution of metal particles within the interlayer PA6 zones of the laminates and the close contact of these particles with the carbon filaments of CFT observed in the RLM and SEM studies (Figs. 3, 4).

As seen from Table 6, increasing the CFT volume fraction in the laminates from 0.25 to 0.50 maintaining the metal concentration results in an increase of the conductivity, in particular in the Cu- and Al-containing laminates.

Figure 7 displays the semi-logarithmic plots of ε' and the $tan\ \delta$ as a function of frequency for the metal-loaded hybrid composites (Fig. 7a, b), for the dually reinforced laminates with $V_f = 0.25$ (Fig. 7c, d) and $V_f = 0.5$ (Fig. 7e, f). At 1 MHz, the ε' of all L-composites displays similar values in the range of 17–21, which is almost independent on the CFT content, the values of the PA6 reference sample being 7–9 (Table 6). Changing the frequency in the 10^2–10^6 range produces relatively few changes. Apparently, at lower frequencies the PA6-metal hybrids without CFT (P-series samples, Fig. 7a) produce higher ε' values than their L-series counterparts. It is to notice in Fig. 7 that an important contribution to the increase of the dielectric constant is also related to increase energy dissipation (and not just to increase in energy storage ability) as shown by the dielectric losses. Thus, the composites with the highest

dielectric constant are also the ones with the higher dielectric loss, i.e., a direct correlation exists between the real part of the electrical conductivity and the dielectric loss given by $\sigma' = \omega.\ \varepsilon'.\ tan\ \delta$ [37].

As to the $tan\ \delta$ values, the hybrids containing 13–19% metal without CFT (Fig. 7b) display notably higher values within the entire frequency range varying from 9 to 1, as compared to the L25 and L50 laminates wherein the respective values are 10–100 times lower (Fig. 7d, f). The lower values of $tan\ \delta$ in the latter case are related with the interfaces established between the metal particles and the carbon fibers. Apparently, these interfaces decrease the mobility of the charge carriers, maintaining them within those interfaces. The micrographs of the L-series obtained by RLM and SEM are in good agreement with these low losses, demonstrating once again a good impregnation of CFT with metal-enriched PA6 materials, i.e., a good affinity between fillers with different nature.

Conclusions

Multiscale laminate composites based on carbon fiber textile structures and PA6 matrices additionally reinforced by metals particles were prepared using microencapsulation strategy. The concentration of the metal particles was 13–19 wt% with respect to the PA6 matrix, the CFT volume fraction reaching 0.5. The preparation route included reactive microencapsulation of the respective metal particles in PA6 capsules by means of anionic polymerization in suspension carried out with commercial monomers and catalysts with possibilities for scale-up. The resulting metal-loaded microcapsules were used for powder impregnation of CFT plies that were subsequently consolidated by conventional compression molding. To the best of our knowledge, such an approach is applied for the first time in the preparation of TPC/CFT laminates with enhanced electrical conductivity. The composites thus obtained displayed a strong increase of the d.c. electrical conductivity in 7 orders of magnitude as well as tunable real component of the dielectric constant and dissipation factor. This effect was accompanied by 2–3 times increase in the Young modulus and ultimate tensile strength as compared to the anionic PA6 matrix. A factor of prime importance to get such behavior was the good distribution of high loads of

metal particles within the PA6 interlayers of the laminates that can be achieved only using the microencapsulated strategy suggested in this work. It is believed that this set of properties quite unusual for traditional TPC/CFT laminates can resolve some problems typical for CFT laminate composites and therefore become a useful platform for structural and functional applications mostly in the automotive and electronic industries.

Acknowledgements

Compliance with ethical standards

Conflict of interest The authors declare that they have no conflicts of interest.

References

[1] Fogel M, Parlevliet P, Olivier P, Dantras É (2017) Manufacturing of conductive structural composites through spraying of CNTs/epoxy dispersions on dry carbon fiber plies. Compos Part A Appl Sci Manuf 100:40–47

[2] Hine PJ, Bonner M, Ward IM et al (2014) Hybrid carbon fibre/nylon 12 single polymer composites. Compos Part A Appl Sci Manuf 65:19–26

[3] Stavrov D, Bersee HEN (2005) Resistance welding of thermoplastic composites-an overview. Compos Part A Appl Sci Manuf 36:39–54

[4] Steenkamer DA, Sullivan JL (1998) On the recyclability of a cyclic thermoplastic composite material. Compos Part B Eng 29:745–752

[5] Chang IY, Lees JK (1988) Recent development in thermoplastic composites: a review of matrix systems and processing methods. J Thermoplast Compos Mater 1:277–296

[6] Khondker OA, Ishiaku US, Nakai A, Hamada H (2005) Fabrication mechanical properties of unidirectional jute/PP composites using jute yarns by film stacking method. J Polym Environ 13:115–126

[7] Svensson N, Shishoo R, Gilchrist M (1998) Manufacturing of thermoplastic composites from commingled yarns: a review. J Thermoplast Compos Mater 11:22–56

[8] Bernet N, Michaud V, Bourban P-E, Månson J-A (2001) Commingled yarn composites for rapid processing of complex shapes. Compos Part A Appl Sci Manuf 32:1613–1626

[9] Sakaguchi M, Nakai A, Hamada H, Takeda N (2000) The mechanical properties of unidirectional thermoplastic composites manufactured by a micro-braiding technique. Compos Sci Technol 60:717–722

[10] van Rijswijk K, Bersee HEN (2007) Reactive processing of textile fiber-reinforced thermoplastic composites: an overview. Compos Part A Appl Sci Manuf 38:666–681

[11] Sekiguchi H, Coutin B (1973) Polymerizability and related problems in the anionic polymerization of lactams. J Polym Sci Polym Chem Ed 11:1601–1614

[12] Provazník M, Puffr R, Šebenda J (1988) Dielectric properties of lactams and their significance in the polymerization process. Eur Polym J 24:511–514

[13] Luisier A, Bourban P-E, Månson J-AE (2003) Reaction injection pultrusion of PA12 composites: process and modelling. Compos Part A Appl Sci Manuf 34:583–595

[14] Cho B-G, McCarthy SP, Fanucci JP, Nolet SC (1996) Fiber reinforced nylon-6 composites produced by the reaction injection pultrusion process. Polym Compos 17:673–681

[15] van Rijswijk K, Bersee HEN, Jager WF, Picken SJ (2006) Optimisation of anionic polyamide-6 for vacuum infusion of thermoplastic composites: choice of activator and initiator. Compos Part A Appl Sci Manuf 37:949–956

[16] van Rijswijk K, Bersee HEN, Beukers A et al (2006) Optimisation of anionic polyamide-6 for vacuum infusion of thermoplastic composites: influence of polymerisation temperature on matrix properties. Polym Test 25:392–404

[17] Harkin-Jones E, Crawford R (1996) Rotational molding of liquid plastic systems: an assessment of material moldability. Adv Polym Technol 15:71–100

[18] Harkin-Jones E, Crawford RJ (1996) Mechanical properties of rotationally molded nyrim. Polym Eng Sci 36:615–625

[19] Ying G, Yang G (2009) Manufacturing and physical properties of all-polyamide composites. J Mater Sci 44:4639–4644. https://doi.org/10.1007/s10853-009-3708-0

[20] Dencheva N, Sampaio AS, Oliveira FM et al (2014) Preparation and properties of polyamide-6-based thermoplastic laminate composites by a novel in-mold polymerization technique. J Appl Polym Sci 131:40083

[21] Guo Z, Sang L, Wang Z et al (2016) Deposition of copper thin films by plasma enhanced pulsed chemical vapor deposition for metallization of carbon fiber reinforced plastics. Surf Coatings Technol 307:1059–1064

[22] Lupoi R, O'Neill W (2010) Deposition of metallic coatings on polymer surfaces using cold spray. Surf Coatings Technol 205:2167–2173

[23] Zhou XL, Chen AF, Liu JC et al (2011) Preparation of metallic coatings on polymer matrix composites by cold spray. Surf Coatings Technol 206:132–136

[24] Che H, Vo P, Yue S (2017) Metallization of carbon fibre reinforced polymers by cold spray. Surf Coatings Technol 313:236–247

[25] Archambault G, Jodoin B, Gaydos S, Yandouzi M (2016) Metallization of carbon fiber reinforced polymer composite by cold spray and lay-up molding processes. Surf Coatings Technol 300:78–86

[26] Kong K, Cheedarala RK, Kim M et al (2016) Electrical thermal heating and piezoresistive characteristics of hybrid CuO–woven carbon fiber/vinyl ester composite laminates. Compos Part A 85:103–112

[27] Oliveira F, Dencheva N, Martins P (2016) Reactive microencapsulation of carbon allotropes in polyamide shell-core structures and their transformation in hybrid composites with tailored electrical properties. EXPRESS Polym Lett 10:160–175

[28] Brêda C, Dencheva N, Lanceros-Mendez S, Denchev Z (2016) Preparation and properties of metal-containing polyamide hybrid composites via reactive microencapsulation. J Mater Sci 51:10534–10554. https://doi.org/10.1007/s10853-016-0274-0

[29] Dencheva N, Denchev Z, Lanceros-Méndez S, Ezquerra Sanz T (2016) One-step in situ synthesis of polyamide microcapsules with inorganic payload and their transformation into responsive thermoplastic composite materials. Macromol Mater Eng 301:119–124

[30] Dencheva NV, Vale DM, Denchev ZZ (2016) Dually reinforced all-polyamide laminate composites via microencapsulation strategy. Polym Eng Sci 57:806–820

[31] Gürdal Z, Haftka RT, Hajela P (1999) Design and optimization of laminated composite materials. Wiley, New York

[32] Dan F, Vasiliu-Oprea C (1998) Anionic polimerization of caprolactama in organic media. Morphological aspects. Colloid Polym Sci 276:483–495

[33] Vasiliu-Oprea C, Dan F (1996) On the relation between synthesis parameters and morphology of anionic polycaproamide obtained in organic media. I. Influence of the Na[O(CH2)2OCH3]2AlH2/isophorone diisocyanate catalytic system. J Appl Polym Sci 62:1517–1527

[34] Ricco L, Monticelli O, Russo S et al (2002) Fast-activated anionic polymerization of ε-caprolactam in suspension, 1. Role of the continuous phase on characteristics and properties of powdered PA6. Macromol Chem Phys 203:1436–1444

[35] Mendes SF, Costa CM, Serra RS et al (2012) Influence of filler size and concentration on the low and high temperature dielectric response of poly(vinylidene fluoride)/Pb(Zr0.53Ti0.47)O3 composites. J Polym Res 19:9967

[36] Lopes AC, Costa CM, Serra RS et al (2013) Dielectric relaxation, ac conductivity and electric modulus in poly(vinylidene fluoride)/NaY zeolite composites. Solid State Ionics 235:42–50

[37] Costa P, Silva J, Lanceros-Méndez S (2016) Strong increase of the dielectric response of carbon nanotube/poly(vinilidene fluoride) composites induced by carbon nanotube type and pre-treatment. Compos Part B Eng 93:310–316